

Electronic and magnetic properties of light rare-earth cubic Laves compounds derived from XMCD experiments

Vilde G. S. Lunde,^{1,*} Benedicte S. Ofstad,¹ Øystein S. Fjellvåg,¹ Philippe Ohresser,² Anja O. Sjåstad,³ Bjørn C. Hauback,¹ and Christoph Frommen^{1,†}

¹*Department for Hydrogen Technology, Institute for Energy Technology, PO Box 40, NO-2027, Kjeller, Norway*

²*Synchrotron SOLEIL, L'Orme des Merisiers, 91190, Saint-Aubin, France*

³*Chemistry Department and Center for Material Science and Nanotechnology, University of Oslo, NO-0315, Norway*

(Dated: November 17, 2025)

This work presents electronic and magnetic properties of selected members in the cubic Laves phase series $\text{Nd}_{1-x}\text{Pr}_x\text{CoNi}$ ($0 \leq x \leq 1$) and $\text{Ce}_{0.25}\text{Pr}_{0.75}\text{CoNi}$, together with the corresponding binary compositions (NdCo_2 , NdNi_2 , PrCo_2 , PrNi_2 , CeCo_2 , CeNi_2), using soft x-ray absorption spectroscopy, x-ray magnetic circular dichroism (XMCD), density-functional theory, and crystal field multiplet calculations. All transition-metal moments saturate below 1 T, while the rare-earth moments do not saturate even at 5 T, consistent with van Vleck paramagnetic contributions and crystal field suppression. While the sum rules are widely used to extract element-specific magnetic moments from XMCD, we show that for $3d$ transition metals, their application requires accurate estimates of the number of unoccupied $3d$ states. We observe a finite magnetic moment on Ni, challenging the common assumption of its nonmagnetic character in Laves phases. The orbital magnetic moments were determined using the spin rules, while the spin moments were estimated from single-ions values from multiplet calculations, due to the invalidity of the spin sum rule for light rare-earth elements. The magnetic moments of Nd and Pr are found to be suppressed relative to their free-ion values, with multiplet theory indicating that this is due to crystal field effects. Our results confirm that Nd and Pr maintain localized $4f^3$ and $4f^2$ configurations, respectively, and that their element-specific magnetic moments are robust to rare-earth substitution. Ce, on the other hand, exhibits a tuneable mixed-valent ground state with both magnetic $4f^1$ and nonmagnetic $4f^0$ components. The relative fraction of these states varies with the electronegativity of the surrounding $3d$ transition metals, revealing a pathway to tune Ce magnetism via composition. This work establishes a framework for accurately interpreting XMCD in light rare-earth-based intermetallics and provides insight for designing light rare-earth-based magnetocaloric materials.

I. INTRODUCTION

Magnetocaloric hydrogen liquefaction (20-80 K) is an alternative to conventional cooling methods at cryogenic temperatures, utilizing the change in magnetic entropy upon magnetization or demagnetization of a magnetic material [1]. Intermetallics based on heavy rare-earth (HRE) elements (Gd-Lu) have been extensively studied for magnetocaloric hydrogen liquefaction due to their large magnetocaloric effect at cryogenic temperatures [2-6]. However, these elements are expensive and classified as critical and strategically important [7], making substitution with light rare-earth (LRE) elements (La-Eu) a necessity, as they are more abundant and less costly [8]. Although LREs generally exhibit weaker magnetic properties than HREs, they can still exhibit significant magnetic moments due to their localized $4f$ electrons. The electronic and magnetic properties of these individual elements can be studied using x-ray absorption spectroscopy (XAS). By varying photon energies across the $L_{2,3}$ edges of $3d$ transition metals, $2p$ core electrons are excited into unoccupied $3d$ valence states [9, 10]. Similarly, on the $M_{4,5}$ edges of rare-earth elements, $3d$ core electrons are

excited into unoccupied $4f$ valence states.

X-ray magnetic circular dichroism (XMCD) can separate the orbital angular momentum μ_L and effective spin angular momentum μ_S^{eff} . As a result of the elemental specificity of XMCD, it is possible to study the influence of substitution on the magnetic moment of the elements. A number of $5f$ actinide-, HRE-, and Sm-based cubic Laves compounds (C15, space group $F\bar{d}\bar{3}m$, No. 227) have previously been studied using XAS and XMCD [11-17]. In contrast, only a few studies on Nd-, Pr-, or Ce-based Laves compounds have been reported, with some exceptions such as CeFe_2 [18, 19] and NdCo_2 (only $L_{2,3}$ -edges of Nd) [20]. Ce can occur in a mixed-valent state, fluctuating between magnetic $4f^1$ and nonmagnetic $4f^0$. The relative occupancy of these two states can be quantified using a lineshape analysis of the Ce XAS spectra [21].

The XMCD method uses the difference in absorption between left $\mu_+(\omega)$ and right $\mu_-(\omega)$ circularly polarized x-rays of a material saturated by an applied magnetic field [22]. μ_L and μ_S^{eff} can be determined by applying the sum rules to the XMCD signal [23, 24]. Various studies have reported different performances of the sum rules, often due to experimental artifacts like saturation effects. Still, reliable comparisons can be made between similar compounds when measured under identical conditions in the same set-up [22, 25]. Additional sources of errors can arise in systems containing multiple phases. For the $L_{2,3}$

* Contact author: vilde.lunde@ife.no

† Contact author: christoph.frommen@ife.no

transitions, the sum rules can be expressed as:

$$\mu_L = -\langle L_z \rangle = -\left(\frac{2q}{3r}\right)n_h, \quad (1)$$

$$\mu_S^{\text{eff}} = 2\langle S_z \rangle + 7\langle T_z \rangle = -\left(\frac{3p - 2q}{r}\right)n_h, \quad (2)$$

and for the $M_{4,5}$ transitions as:

$$\mu_L = -\langle L_z \rangle = -\left(\frac{q}{r}\right)n_h, \quad (3)$$

$$\mu_S^{\text{eff}} = 2\langle S_z \rangle + 6\langle T_z \rangle = -\left(\frac{5p - 3q}{2r}\right)n_h, \quad (4)$$

where p is the integral of the XMCD signal over the L_3 or M_5 peak, q is the integrated XMCD signal over the $L_{2,3}$ or $M_{4,5}$ peaks, and n_h is the number of holes in the $3d$ or $4f$ shell [22]. The r is the integrated difference between the average XAS signal of μ_+ and μ_- and a step function with two steps [22]. However, this approximation can lead to an underestimation of the magnetic moment, in particular for rare-earth elements [26]. The $\langle L_z \rangle$, $\langle S_z \rangle$, and $\langle T_z \rangle$ are the expectation values of the orbital, spin, and intra-atomic magnetic dipole operators, respectively. The $\langle T_z \rangle$ is generally considered negligible for powders [27].

Determining n_h is straightforward for species with integer-valued electron configurations, *i.e.*, the number of $4f$ holes of Nd and Pr. For itinerant species, however, n_h cannot be measured directly. As a result, most studies omit reporting the n_h used or report widely different values. For example, the number of $3d$ holes, n_h , for Co in ErCo_2 has been estimated as 1.1 through fitting of XMCD data to match bulk magnetization data [15]. In contrast, another study has obtained n_h of 2.49 for elemental Co based on averaging reported theoretical calculations [22]. This resulted in magnetic moments of $0.81 \mu_B$ and $1.75 \mu_B$, respectively. However, the corresponding magnetic moments per hole are similar (0.70 and $0.74 \mu_B/n_h$, respectively). This highlights the importance of accurately estimating n_h since it linearly scales μ_L and μ_S^{eff} derived from the sum rules.

Using the spin sum rule, the spin moment $\mu_S = 2\langle S_z \rangle$ can be reliably determined for $3d$ transition metals [22, 28], while for LREs, $3d$ - $4f$ exchange interactions and $3d$ core spin-split interaction induce significant deviations [29, 30]. Furthermore, crystal field effects have a significant impact on the calculated LRE magnetic moments using the sum rules.

We have previously investigated the magnetocaloric effect in cubic Laves phase compounds with the general formula AB_2 . In that study, we focused on three different LREs, Nd, Pr, and Ce, occupying the A-site, while the B-site was occupied by an equimolar ratio of Co and Ni [31]. Magnetic measurements show that the compounds exhibit ferromagnetic ordering at low temperatures, except CeCoNi and $\text{Ce}_{0.75}\text{Pr}_{0.25}\text{CoNi}$ [31]. In the present work,

we have used XAS and XMCD to investigate the electronic and magnetic properties of these LRE-based cubic Laves compounds in detail.

The paper is organized as follows. Section II describes the experimental and computational methods used in this study. Section III presents the results of the structural analysis, as well as the electronic and magnetic properties of the compounds.

II. METHODS

A. Experimental

An overview of the compounds investigated in this study is tabulated in Table I. All samples were prepared by arc melting and heat-treated using the protocol as previously described [31]. The compounds were stored under an Ar atmosphere to prevent oxidation. Crystal structures were investigated by x-ray diffraction (XRD) using a Bruker D2 diffractometer in Bragg-Brentano geometry (Cu-K α radiation, $\lambda = 1.54060 \text{ \AA}$) at room temperature (RT). Rietveld refinements were performed using Topas V5 [32].

TABLE I: Compounds investigated in this study.

Ternary and quaternary alloys*	Binary alloys
NdCoNi	NdCo_2
$\text{Nd}_{0.75}\text{Pr}_{0.25}\text{CoNi}$	NdNi_2
$\text{Nd}_{0.50}\text{Pr}_{0.50}\text{CoNi}$	PrCo_2
$\text{Nd}_{0.25}\text{Pr}_{0.75}\text{CoNi}$	PrNi_2
PrCoNi	CeCo_2
$\text{Ce}_{0.25}\text{Pr}_{0.75}\text{CoNi}$	CeNi_2

*Samples reused from [31].

XAS and XMCD measurements were carried out at the CroMag end station, DEIMOS beamline at the SOLEIL synchrotron facility, France [33, 34]. Data were collected in the Total Electron Yield (TEY) mode, with an energy resolution of more than $E/\Delta E = 5000$, and circularly polarized light. Finely crushed sample powder was placed on an $8 \times 8 \text{ mm}$ carbon tape attached to a Cu sample holder under ambient air. The samples were exposed to air for 5-10 minutes before being transferred to an ultra-high vacuum at a temperature of 4.2 K, and thus below the Curie temperature of the compounds [31]. The XAS spectra were recorded at $\pm 5 \text{ T}$. All edges (Ni, Co, Ce, Pr, Nd) were measured for all samples and binaries listed in Table I, except Ni, which was measured only for NdCoNi , PrCoNi , and the binaries. Typically, 18 scans were performed per set of edges, and their average was determined, normalized by their pre-edge. Finally, the XAS and XMCD spectra were calculated from the average and difference between μ_+ and μ_- , respectively.

For each polarization, field-dependent measurements were performed at 4.2 K from -5 T to $+5 \text{ T}$ at the en-

ergy corresponding to the strongest XMCD signal of the L_3 or M_5 edges. The energies used for Co, Ni, Ce, Pr, and Nd were 781.8, 855.9, 903.3, 953.4, and 1004.1 eV, respectively. The corresponding magnetization curves were constructed from the field-dependent XMCD signal and scaled using the total magnetic moments obtained from the sum rules at 5 T. The data points close to zero field were removed since they resulted from strong perturbations of TEY in this range.

B. Computational

Ab initio spin-polarized density-functional theory (DFT) calculations were performed with the Vienna *Ab Initio* Simulation Package, VASP 6.4.1 [35–37], within the scalar relativistic approximation including spin-orbit coupling using the SCAN-L [38] meta-GGA functional. The Brillouin zone was sampled using a Monkhorst-Pack [39] $11 \times 11 \times 11$ k -point grid, and a plane-wave cutoff energy of 550 eV was employed. A total of 60 bands were included in the calculation, with electronic self-consistency achieved to a convergence threshold of 10^{-6} eV per supercell. Structural optimization with a force tolerance criterion of 0.01 eV/Å was conducted for all the materials. To correct for on-site electron-electron interactions in localized d - and f -orbitals, the Hubbard U method was employed. The values of U were estimated using the linear response approach of Cococcioni and de Gironcoli [40].

Full multiplet calculations within the crystal field regime were constructed using QUANTY [41]. Values for the Slater integrals and spin-orbit coupling constants were obtained from Cowan's Hartree-Fock code [42] and subsequently scaled by 90% of their values to account for configuration interaction effects. The coefficients were optimized to reproduce the XMCD spectra and were restricted by the orbital moment calculated from the orbital sum rules. For a more detailed description of the methodology, refer to the Supplemental Material [43].

III. RESULTS

A. Structural analysis

The $\text{Nd}_{1-x}\text{Pr}_x\text{CoNi}$ ($0 \leq x \leq 1$) and $\text{Ce}_{0.25}\text{Pr}_{0.75}\text{CoNi}$ compounds investigated in this work were reused from [31]. Combined XRD and SEM-EDS analyses confirmed that the compounds exhibit the cubic Laves phase with minor AB or AB_3 secondary phases. The XRD results of the binaries synthesized for this work are reported in the Supplemental Material [43]. Rietveld refinements confirm that all compounds primarily consist of the cubic AB_2 Laves phase. Nd- and Pr-based binaries exhibit some secondary AB or AB_3 phases (0.8–6.5 wt%). The Ce-based compounds exhibit significant oxidation due to

air exposure, consistent with previous observations for CeCoNi [31].

B. Electronic properties

The XAS and corresponding XMCD spectra for the $L_{2,3}$ edges of Co and Ni and the $M_{4,5}$ edges of Nd and Pr are presented in Fig. 1 and in the Supplemental Material [43]. The Co-edges (Fig. 1(a)) display L_3 and L_2 peaks at 781.3 eV and 796.5 eV, respectively. As expected, the L_3 peak is more intense. A small shoulder can be observed on the right side of the L_3 peak, possibly as a result of surface oxidation. Two additional peaks appear at energies higher than the main peaks of Co (787.3 eV and 802.1 eV) in the NdCoNi spectrum, and weaker peaks at the same energies are barely visible in the $\text{Nd}_{0.75}\text{Pr}_{0.25}\text{CoNi}$ spectrum. These features appear at the energies corresponding to Ba with the expected branching ratio, making Ba contamination from the sample holder a possible explanation. As these features are assumed to result from contamination, their contributions to the XAS signal were not included in the sum rule analysis and could not influence the results. Aside from these additional features, the Co XAS spectra are consistent across all samples.

The Ni-edges of NdCoNi and PrCoNi (Fig. 1(b)) show the L_3 and L_2 peaks at 855.8 and 873.2 eV, respectively. The XAS signal does not differ between these two samples or their corresponding binary samples, indicating no significant variation in the Ni electronic environment. A minor satellite peak is present at a higher energy than the L_3 peak (\sim 862 eV) for all samples. This was also observed for Ni in the cubic Laves phase GdNi_2 [12], which was attributed to the $2p^5d^9$ configuration.

The $M_{4,5}$ edges of Nd and Pr (Fig. 1(c-d)) exhibit multiple peaks, which is common for $4f$ elements due to the strong $4f$ localization giving rise to $3d$ - $4f$ and $4f$ - $4f$ interaction, resulting in a multiplet-level splitting of the quasi-atomic initial and final states [23]. The multiplet structure appears systematic for the series. The multiplets are well resolved, indicating a lack of $4f$ - $3d$ hybridization. This is further confirmed by DFT calculations, which indicate that the f -electron valency is given as an integer number for both Nd and Pr. Furthermore, the partial density of states plot for $\text{Nd}_{0.50}\text{Pr}_{0.50}\text{CoNi}$, found in the Supplementary Material [43], reveals highly localized f -electrons with minimal overlap with the Co and Ni d -states.

For all the Nd-edges (Fig. 1(c)), the M_5 peak at 982.1 eV features a small low-energy shoulder, while the M_4 edge displays multiple peaks at 999.7, 1001.8, and 1003.8 eV. The XAS spectra are consistent for all samples, including the binaries. Nd exhibits a $4f^3$ electron configuration, according to reported calculations and experiments with identical XAS spectra [23, 44, 45]. Furthermore, the Pr-edges (Fig. 1(d)) show an M_5 peak (932.9 eV) with a shoulder at lower energies and an

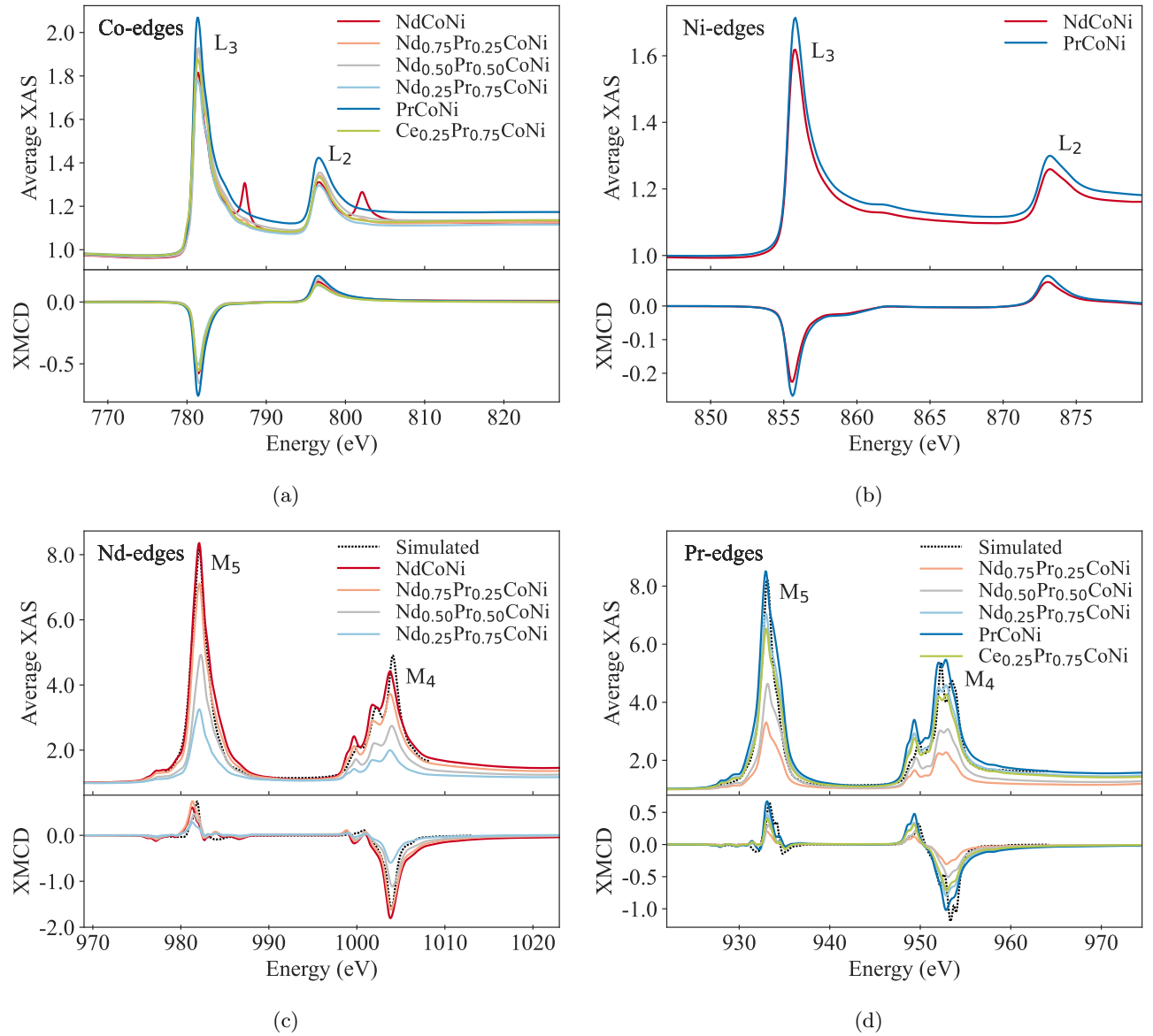


FIG. 1: (a) Co and (b) Ni experimental $L_{2,3}$ and (c) Nd and (d) Pr simulated and experimental $M_{4,5}$ edges measured at 4.2 K and 5 T. The XAS spectra represents the average of the left and right polarized x-ray absorption, while XMCD shows the difference.

M_4 edge consisting of multiple peaks (949.3, 952.0, and 952.8 eV). Again, the signal is similar for all samples. Reported calculations and experiments indicate that Pr exhibits a $4f^2$ electron configuration [23, 44, 45]. The electron configurations and spectra of Nd and Pr were confirmed using DFT calculations and multiplet theory simulations of the XAS and XMCD spectra.

C. Magnetic properties

All measured edges (Co, Ni, Ce, Pr, Nd) for the studied compounds produce XMCD signals, as seen in Fig. 1.

The strongest XMCD peaks relative to the strength of the XAS were observed at the Co-edge, followed by the Nd-, the Pr-, Ni-, and Ce-edges, respectively.

Figure 2 shows the results of the sum rule calculations for $Nd_{1-x}Pr_xCoNi$, while the magnetic moments for all studied compounds are tabulated in Supplemental Material [43]. $\langle T_z \rangle = 0$ is assumed for the sum rule analysis since the compounds are powders [27]. The Pr and Nd μ_S were estimated from the single-ion values from our crystal electric field model due to the invalidity of the spin sum rule for LREs, and values obtained using this sum rule are tabulated in the Supplemental Material [43] for comparison. The model assumes a cubic crystal field and was constrained by the XMCD data and the orbital

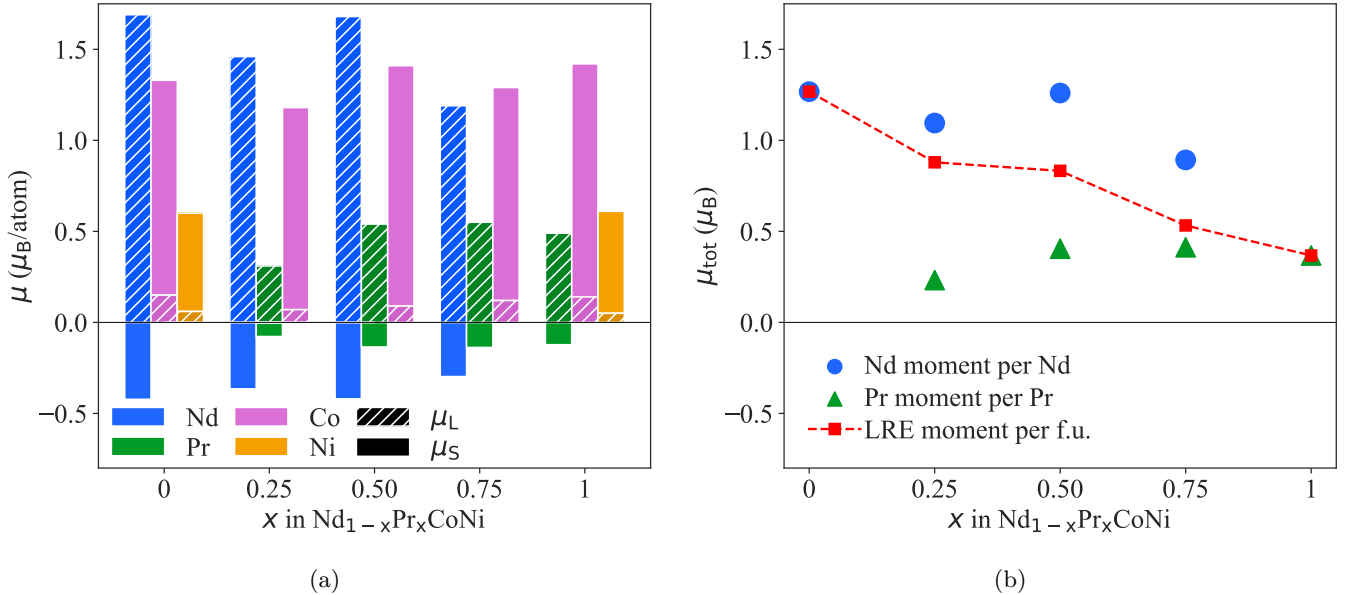


FIG. 2: (a) The orbital (hatched) and spin (filled) moment for Nd, Pr, Co, and Ni. Ni was only measured for NdCoNi and PrCoNi . μ_S for Pr and Nd was calculated using multiplet theory, while all other values are found by applying the sum rules to the experimental XMCD data. (b) The total magnetic moment of Nd and Pr per atom, together with the total LRE moment per formula unit.

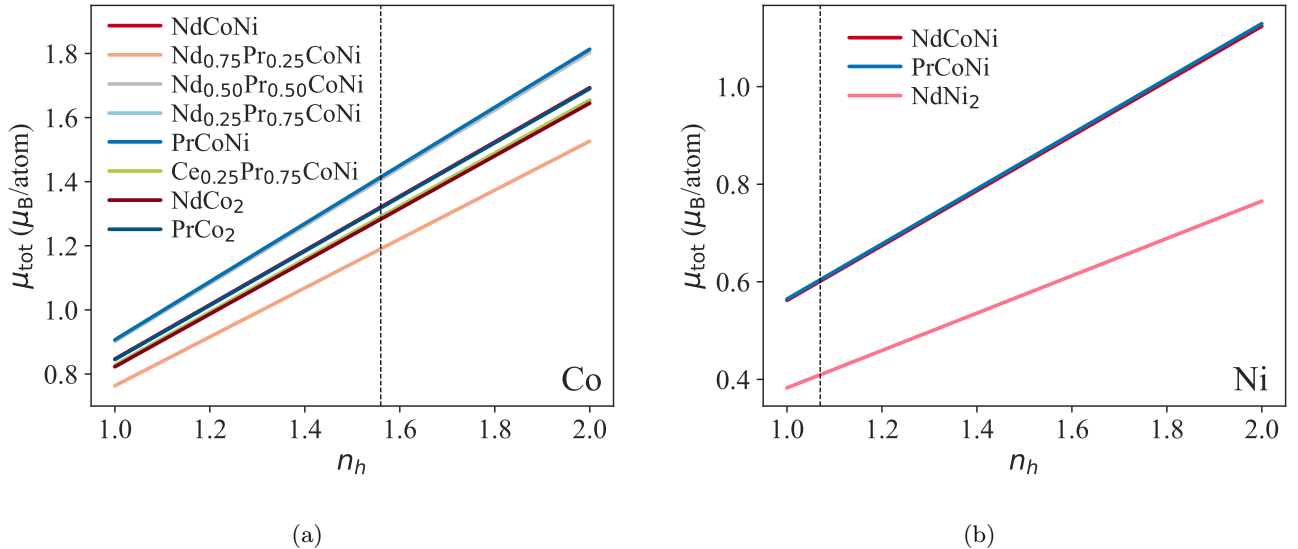


FIG. 3: The total Co and Ni moment as a function of the n_h chosen in the sum rules. The n_h determined using DFT calculations in this work are shown with a vertical line for each of the edges.

moment calculated according to the orbital sum rule. All other values are found by applying the sum rules to experimental XMCD data. The magnetic moments were only calculated for the binary samples expected to exhibit magnetic ordering at 4.2 K, i.e., NdCo_2 , NdNi_2 , and PrCo_2 , and not for the paramagnetic compounds (PrNi_2 , CeCo_2 , and CeNi_2) [46]. Figure 2(a) shows μ_L and μ_S for Nd, Pr, Co, and Ni in $\text{Nd}_{1-x}\text{Pr}_x\text{CoNi}$. Figure

2(b) shows the total magnetic moments of Pr and Nd for $\text{Nd}_{1-x}\text{Pr}_x\text{CoNi}$ together with the summed LRE magnetic moments per formula unit. All elements exhibit a finite magnetic moment. There is no clear trend for the Co magnetic moment based on the LRE composition, and the variation between the samples of $\pm 0.10 \mu_B/\text{atom}$ is less than the error bar associated with XMCD and sum rule analysis. The magnetic moment of Ni is similar for

NdCoNi and PrCoNi (0.60 and 0.61 μ_B , respectively).

The n_h for 3d transition metal itinerant species is typically obtained by subtracting the number of d -electrons from the total number of available d -states. We calculated the number of electrons from the partial electronic density of states calculated by DFT. When subtracting these values from the number of d -states, we obtain values of 2.66 for Co and 1.34 for Ni. These values are similar to some values reported in the literature, *e.g.* 2.49 and 1.59 for Co and Ni, respectively [12, 22]. However, this approach overestimates the magnetic moment for our samples compared to magnetization data.

If we calculate n_h by projecting the DFT ground-state electron density onto spherical harmonics and integrating the partial electronic density of states above the Fermi level, we obtain lower values, around 1.56 for Co and 1.07 for Ni. The latter approach is physically more meaningful as it is n_h we aim to obtain. It is thus more correct, and we use these values in our analysis. The dependence of the moment as a function of n_h for these elements is shown in Fig. 3, highlighting the importance of an accurate estimation of this parameter for comparing moments across different studies and experimental techniques.

The n_h for Pr and Nd were determined to be integer numbers of 12 and 11, respectively, based on the XAS spectra and DFT calculations.

The magnetic moments of Co and Ni saturate around 0.5 T, while those of the LREs remain unsaturated at 5 T, the maximum field applied, as seen in Fig. 4. Consequently, the results derived using the sum rules in this work correspond to the values at 5 T, which do not represent the full saturation moments for the LREs. TEY was used as a probe, measuring both the 3d transition metal and LRE edges on the order of a few nanometers, making the results sensitive to the surface, regardless of the element. The lack of saturation in the magnetization may be attributed to van Vleck paramagnetism, which arises from the mixing of higher multiplets with the ground state, yielding a linear contribution as a function of the applied field [47].

The total magnetization of the elements in the compounds is compared to bulk magnetization measurements from our previous study [31] in Fig. 5. Ni saturates at low field (Fig. 4), and when this contribution is added to the samples where the Ni edge was not measured, the XMCD signal for the samples becomes slightly more saturated. The remaining discrepancies between the two measurement techniques may be attributed to mild surface oxidation at ambient temperature during sample handling, forming a poorly crystalline layer of antiferromagnetic or paramagnetic contributions. However, the absence of an exchange bias shift in the XMCD curves suggests oxidation to be limited [48].

There is a difference in hysteresis between bulk and XMCD magnetization for some of the samples. Part of this discrepancy can be attributed to that data points close to zero field have been removed from the XMCD results due to strong perturbations of TEY at these values.

However, for $\text{Nd}_{0.75}\text{Pr}_{0.25}\text{CoNi}$, the difference is larger than what can be attributed to this explanation. This difference could be caused by the differences between the two measurement techniques, involving probing either the bulk or the surface. The exact same samples were characterized using the two techniques, eliminating the possibility of differences in saturation and hysteresis due to poor reproducibility in the sample preparation.

The magnetic moments of Co and Ni (1.2-1.4 and 0.4-0.6 μ_B , respectively) are significantly smaller than those calculated from the free ions using Hund's rules (6.75 and 6.00 μ_B , respectively). The magnetism of the 3d transition metals results from unpaired 3d-electrons, and μ_L is often quenched compared to what is calculated for the magnetic ground state using Hund's rules [49]. This was observed for Co and Ni, where μ_L is close to zero, and the moment mainly results from μ_S . Transition metal magnetic moments generally couple ferromagnetically to the LRE moments in cubic Laves compounds but antiferromagnetically to HRE moments [5, 46, 50]. Ferromagnetic coupling is observed in this system, for all elements exhibiting μ_{tot} parallel to the applied field. The LRE moment is not constant upon transition metal substitution.

As expected, Co exhibits a higher magnetic moment than Ni. However, Ni is generally assumed to exhibit a small or no magnetic moment in cubic Laves compounds [6], and has been reported as nonmagnetic for CeNi_2 , NdNi_2 , and PrNi_2 [46]. In this study, we observe a finite magnetic moment for Ni in all evaluated compounds, with a μ_{tot} of 0.41 μ_B for NdNi_2 , contradictory to previous reports [46]. For GdNi_2 Laves phases, Ni has a moment of 0.2 μ_B antiparallel to Gd, determined using XMCD at 1.4 T and 25 K [12]. This magnetic moment is significantly smaller than what we have observed (0.4-0.6 μ_B), but this can be attributed to the differences in the applied field and temperature being used. To the best of our knowledge, the magnetic moment of Co in LRE Laves phases has not previously been determined using the sum rules. However, for ErCo_2 a Co moment of 0.9-1.0 μ_B has been found at 1 T [15, 16]. The Co magnetic moment of NdCo_2 has been studied using neutron diffraction, where the Co moment has been determined in the range 0.51-0.86 μ_B [51]. As previously discussed, part of these discrepancies could be attributed to different choices of n_h .

For the LREs, μ_L is significantly higher than μ_S and oppositely directed, as expected based on Hund's rules. Magnetic moments calculated using Hund's rules for free trivalent ions, $\mu = g_J J \mu_B$, for Nd (3.27 μ_B) and Pr (3.20 μ_B) are higher than the magnetic moments derived in this work, 0.89-1.26 μ_B and 0.24-0.41 μ_B , respectively. The low values for the LREs are most likely due to the lack of saturation in the magnetization at 5 T (see Fig. 4). A further reduction of the Pr moment compared to the Nd magnetic moment can be attributed to crystal field effects. Nd has a significantly higher μ_{tot} than Pr, resulting in an almost linear decrease in μ_{tot} per formula unit for $\text{Nd}_{1-x}\text{Pr}_x\text{CoNi}$ ($0 \leq x \leq 1$) with increasing Pr

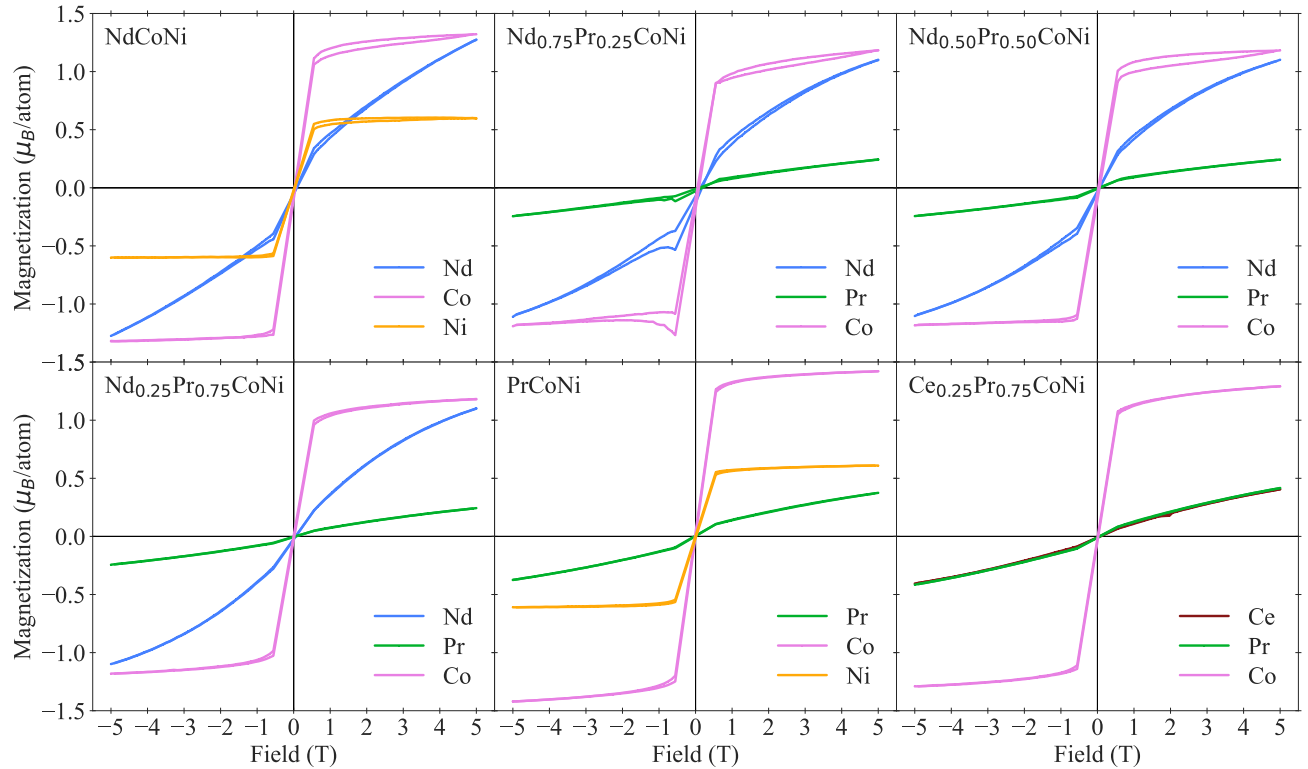


FIG. 4: Field-dependent XMCD measurements performed at 4.2 K, at the energy of the strongest peak for each edge. The curves are scaled using the results from the sum rules at 5 T. Data points close to zero field have been removed.

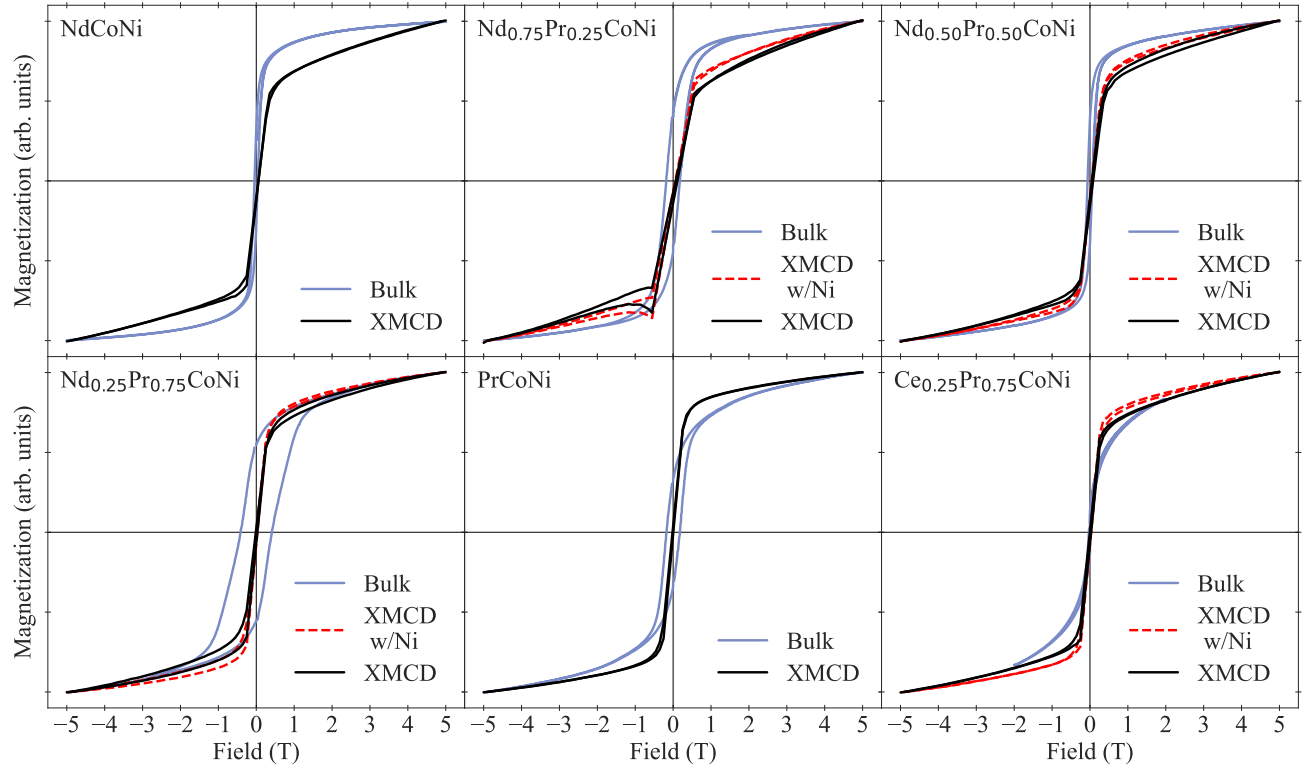


FIG. 5: Normalized field-dependent magnetization curves measured using bulk magnetization measurements at 5 K [31] and XMCD, as the sum of the field-dependent magnetization of all the measured edges in Fig. 4. For compounds where the Ni edge was not measured, the Ni contribution from NdCoNi is added as dashed curves.

substitution (Fig. 2(b)). The magnetic moment per Nd and Pr atom is quite similar for all the compounds and is not significantly influenced by the substitution. For comparison, the μ_S values of Pr and Nd obtained using the invalid LRE spin sum rule are significantly higher than those obtained using multiplet theory calculations. This results in a negative μ_{tot} for all compounds using these values.

Bulk magnetization data for PrCoNi and NdCoNi yield magnetic moments of 2.2 and 2.4 μ_B , respectively. In comparison, the total moments obtained from the XMCD data for these compounds are 2.5 and 3.6 μ_B , respectively. Consequently, the moments derived from XMCD data are overestimated compared to the bulk magnetization data. The magnetic moments obtained from XMCD might be influenced by surface oxidation due to the low penetration depth of TEY. Possible surface oxides of Pr, Nd, Co, and Ni are paramagnetic or antiferromagnetic at the measurement temperature of 4.2 K [52–55]. However, the larger magnetic moments obtained by XMCD compared to bulk magnetization could indicate that any surface oxidation is likely limited.

D. Cerium electronic and magnetic properties

Figure 6 presents the XAS and XMCD spectra of the Ce-edge for $Ce_{0.25}Pr_{0.75}CoNi$, with the binary samples $CeCo_2$ and $CeNi_2$ included for comparison. Both the M_5 and M_4 edges consist of multiple peaks. The three most intense M_5 peaks are at 884.7, 885.7, and 887.1 eV, and the two most dominant M_4 peaks are at 903.0 and 904.7 eV. Both edges contain shoulders at higher and lower energies than the main peaks.

Some of the peaks correspond to magnetic $4f^1$ ($J = 5/2$) Ce states, while others correspond to nonmagnetic $4f^0$ ($J = 0$) Ce states, resulting in changing XMCD signals. The XAS signal evolves significantly along the series ($Ce_{0.25}Pr_{0.75}CoNi$, $CeCo_2$, and $CeNi_2$) as the ratio between the different peaks varies, indicating changes in the $4f^1/4f^0$ ratio. The $4f^0$ are shifted to higher energies for all compounds to reduce electron screening, resulting in tighter binding to the core levels [56].

To approximate the $4f^1/4f^0$ ground state ratio, a line-shape analysis was employed on the M_4 edges [57], shown in Fig. 7. It should also be underlined that the lineshape analysis does not differentiate between Ce $4f^0$ and $4f^1$ in the main Laves phases and in a secondary phase. The average XAS and the XMCD spectra were fitted using spectra simulated from the Ce $4f^1$ and Ce $4f^0$ configurations, as calculated through multiplet theory. These spectra were integrated to determine the fractions of $4f^1$ and $4f^0$. This analysis revealed a $4f^1:4f^0$ ratio of 1:1 for $CeCo_2$, 2:3 for $CeNi_2$, and 1:2 for $Ce_{0.25}Pr_{0.75}CoNi$. This confirms the high presence of nonmagnetic Ce $4f^0$ in the Ce-containing samples, as expected based on the small lattice constants and low bulk magnetization of $Ce_{1-x}Pr_xCoNi$ ($0.25 \leq x \leq 1$) compounds in our previ-

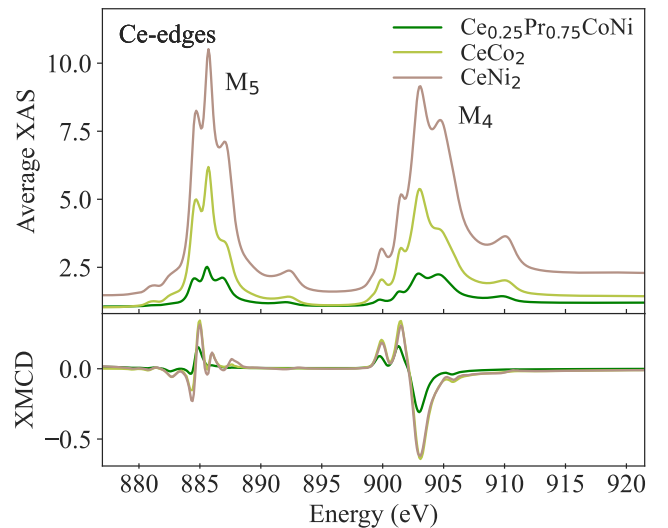


FIG. 6: Ce $M_{4,5}$ edges measured at 4.2 K and 5 T. XAS shows the average of the right and left polarized x-ray absorption, while XMCD shows the difference.

ous study [31]. This is further supported by the smaller lattice constants of $CeCo_2$ (7.16 Å) and $CeNi_2$ (7.22 Å) compared to $PrCo_2$ (7.31 Å) and $PrNi_2$ (7.29 Å) in the present study. Liu *et al.* [58] observed increasing lattice parameters from Pr to Ce in $Pr_{1-x}Ce_xAl_2$, indicating a dominant $4f^1$ configuration. This suggests Ce exhibits a higher fraction of $4f^1$ configuration in cubic Laves compounds with Al at the B-site than with Ni and Co at the B-site. This could be a result of the higher electronegativity of Co (1.88) and Ni (1.91) compared to Al (1.61). The Ce-edge of $Ce_{0.25}Pr_{0.75}CoNi$ exhibits the strongest XMCD signal relative to the XAS signal out of the three compounds, despite the lowest fraction of $4f^1$ configuration. This is possibly due to the fact that this compound is ferromagnetically ordered. Both $CeCo_2$ and $CeNi_2$ are paramagnetic at the measured temperature (4.2 K), while $Ce_{0.25}Pr_{0.75}CoNi$ orders ferromagnetically at 11 K, which will give a stronger ordering of the magnetic moments and provide a higher XMCD signal.

For the sum rules, the $4f^1$ configuration is assumed for Ce, since the $4f^0$ configuration does not contribute to the magnetic moment, resulting in $n_h = 13$. This choice of n_h is consistent with what has been published for mixed-valent Ce [57]. As previously pointed out, the spin sum rule is not reliable for LREs. Additionally, the spin sum rule (Eq 4) requires well-separated M_4 and M_5 edges, which is not the case for Ce (Fig. 6(a)). Therefore, only μ_L was determined experimentally using the sum rules. As for Nd and Pr, the μ_L ($0.53 \mu_B$) is parallel to the applied field, and the calculated μ_S ($0.13 \mu_B$) is antiparallel and smaller, resulting in a μ_{tot} ($0.40 \mu_B$) parallel to the field. The Ce moment is calculated per Ce, not per Ce $4f^1$. There is a surprisingly small difference

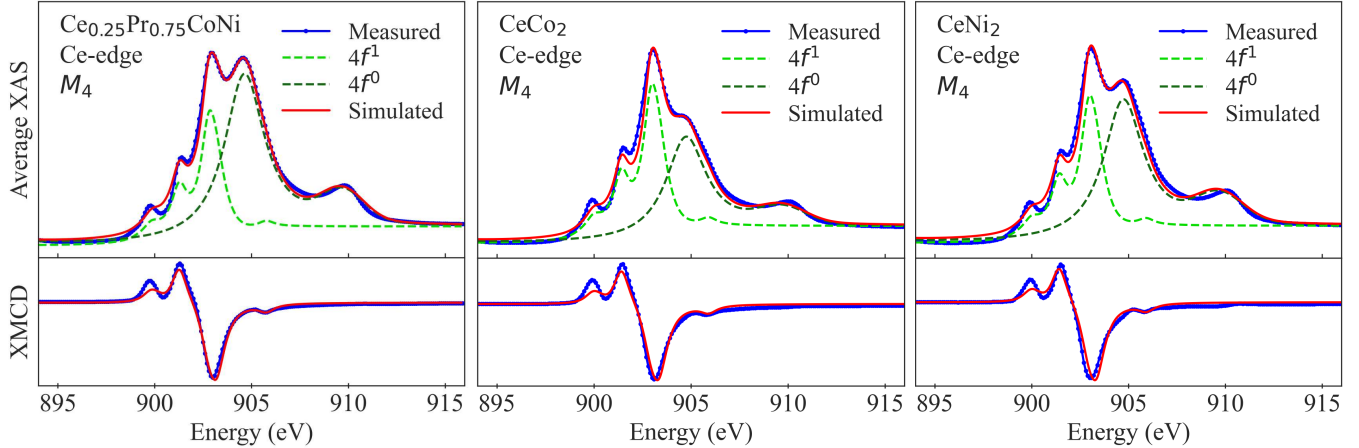


FIG. 7: Lineshape analysis of the experimental M_4 edge of Ce, used to determine the fraction of $4f^0$ and $4f^1$ using multiplet theory simulations. The simulated curve is the sum of the $4f^0$ and $4f^1$ contributions, fitted to the background-corrected experimental data. For the XMCD signal, only $4f^1$ contributes to the signal and is simulated.

in magnetic moment between Pr and Ce, considering the difference measured in the compounds using magnetization measurements [31]. Ce $4f^1$ has a calculated μ using Hund's rules of $2.14 \mu_B$, while Ce $4f^0$ has $0 \mu_B$ [49]. Based on the fraction of Ce $4f^1$ and Ce $4f^0$ estimated from the lineshape analysis, the low magnetic moment determined from the sum rules indicates that the Ce moment is suppressed by the lack of saturation and crystal field effects, similarly to the Pr and Nd moments.

5 T. This can be attributed to van Vleck paramagnetism, which provides a linear contribution as a function of the field.

We found that Ce in the cubic Laves compounds consists of between 50 and 66% of nonmagnetic Ce $4f^0$ ($J = 0$) and between 50 and 34% of magnetic Ce $4f^1$ ($J = 5/2$), with the fractions being dependent on the electronegativity of the $3d$ transition metals in the compound. This tunability of magnetic Ce is important as Ce is the most abundant of the LRE elements.

IV. CONCLUSIONS

In this work, we used soft x-ray absorption spectroscopy to investigate the electronic and magnetic properties of LRE-based $Nd_{1-x}Pr_xCoNi$ ($0 \leq x \leq 1$) and $Ce_{0.25}Pr_{0.75}CoNi$ cubic Laves phase compounds together with the corresponding binary compounds for magnetocaloric applications. The experimental results are supported by density-functional theory calculations, which enable the calculation of the number of holes.

Ni and Co exhibited a slightly larger magnetic moment than expected (0.4 - 0.6 and 1.2 - $1.4 \mu_B$, respectively), whereas the magnetic moments of the LRE elements were suppressed by the crystal field. The magnetic moments of the $3d$ transition metals saturate at low magnetic fields. In contrast, the magnetic moments of the LRE elements did not reach a flat saturation plateau at

ACKNOWLEDGMENTS

This work was financed by the Research Council of Norway under project number 336403. Experiments were performed on the DEIMOS beamline at SOLEIL Synchrotron, France (proposal number 20240548). We are grateful to the SOLEIL staff for their smooth operation of the facility. Calculations were performed on resources provided by Sigma2—the National Infrastructure for High Performance Computing and Data Storage in Norway, Grant No. NN11060K.

DATA AVAILABILITY

The data that support the findings of this article are openly available [59].

[1] V. Franco, J. Blázquez, J. Ipus, J. Law, L. Moreno-Ramírez, and A. Conde, Magnetocaloric effect: From materials research to refrigeration devices, *Progress in Materials Science* **93**, 112 (2018).

[2] C. Romero-Muñiz, J. Y. Law, J. Revuelta-Losada, L. M. Moreno-Ramírez, and V. Franco, Magnetocaloric materials for hydrogen liquefaction, *The Innovation Materials* **1**, 100045 (2023).

[3] P. K. Jesla, J. A. Chelvane, A. V. Morozkin, and R. Nirmala, Large Low Field Magnetocaloric Effect in Multicomponent Laves Phase Intermetallic Compounds $Gd_{0.33}Dy_{0.33}Ho_{0.33}Al_2$, $Tb_{0.33}Ho_{0.33}Er_{0.33}Al_2$, and $Dy_{0.33}Ho_{0.33}Er_{0.33}Al_2$, *IEEE Transactions on Magnetics* **59**, 1 (2023).

[4] J. Ćwik, Y. Koshkid'ko, K. Shinde, J. Park, N. A. De Oliveira, M. Babij, and A. Czernuszewicz, Magnetic and magnetocaloric properties of $Dy_{1-x}Er_xNi_2$ solid solutions and their promise for hydrogen liquefaction, *Journal of Materials Chemistry C* **12**, 14421 (2024).

[5] G. Politova, I. Tereshina, A. Karpenkov, V. Chzhan, and J. Cwik, Magnetism, magnetocaloric and magnetostrictive effects in RCo_2 – type (R = Tb, Dy, Ho) Laves phase compounds, *Journal of Magnetism and Magnetic Materials* **591**, 171700 (2024).

[6] E. Bykov, A. Karpenkov, W. Liu, M. Straßheim, T. Niehoff, K. Skokov, F. Scheibel, O. Gutfleisch, C. Salazar Mejía, J. Wosnitza, and T. Gottschall, Magnetocaloric effect in the Laves phases RCo_2 (R = Er, Ho, Dy, and Tb) in high magnetic fields, *Journal of Alloys and Compounds* **977**, 173289 (2024).

[7] EU, Regulation (EU) 2024/1252 of the European parliament and of the council of 11 April 2024 establishing a framework for ensuring a secure and sustainable supply of critical raw materials (2024).

[8] W. Liu, T. Gottschall, F. Scheibel, E. Bykov, A. Aubert, N. Fortunato, B. Beckmann, A. M. Döring, H. Zhang, K. Skokov, and O. Gutfleisch, A matter of performance and criticality: A review of rare-earth-based magnetocaloric intermetallic compounds for hydrogen liquefaction, *Journal of Alloys and Compounds* **995**, 174612 (2024).

[9] P. Ohresser, N. B. Brookes, S. Padovani, F. Scheurer, and H. Bulou, Magnetism of small Fe clusters on Au(111) studied by x-ray magnetic circular dichroism, *Physical Review B* **64**, 104429 (2001).

[10] G. Van Der Laan and A. I. Figueroa, X-ray magnetic circular dichroism—A versatile tool to study magnetism, *Coordination Chemistry Reviews* **277-278**, 95 (2014).

[11] C. Giorgetti, E. Dartyge, F. Baudelet, and R.-M. Galéra, XMCD at the $Li_{ii,iii}$ edges of Er in $ErMn_2$, $ErFe_2$, $ErCo_2$, $ErNi_2$, and $ErAl_2$ Laves phases and in $Er_2(SO_4)_3 \cdot 8H_2O$, *Physical Review B* **70**, 035105 (2004).

[12] M. Mizumaki, K. Yano, I. Umehara, F. Ishikawa, K. Sato, A. Koizumi, N. Sakai, and T. Muro, Verification of Ni magnetic moment in $GdNi_2$ Laves phase by magnetic circular dichroism measurement, *Physical Review B* **67**, 132404 (2003).

[13] F. Wilhelm, R. Eloirdi, J. Rusz, R. Springell, E. Colineau, J.-C. Griveau, P. M. Oppeneer, R. Caciuffo, A. Rogalev, and G. H. Lander, X-ray magnetic circular dichroism experiments and theory of transuranium Laves phase compounds, *Physical Review B* **88**, 024424 (2013).

[14] A. Fujiwara, K. Asakura, I. Harada, H. Ogasawara, and A. Kotani, XMCD Study on Electronic and Magnetic States of RareEarth 5d Electrons in Laves Compounds, RFe_2 (R = Rare-Earth), *Physica Scripta* , 113 (2005).

[15] F. Bartolomé, J. Herrero-Albillas, L. García, A. Young, T. Funk, N. Plugaru, and E. Arenholz, Orbital moment at the Curie temperature in $ErCo_2$, *Journal of Magnetism and Magnetic Materials* **272-276**, 319 (2004).

[16] J. Herrero-Albillas, F. Bartolomé, L. M. García, A. T. Young, T. Funk, J. Campo, and G. J. Cuello, Observation of a different magnetic disorder in $ErCo_2$, *Physical Review B* **76**, 094409 (2007).

[17] S. Watanabe, N. Ishimatsu, H. Maruyama, J. Chaboy, M. A. Laguna-Marco, R. Boada, and N. Kawamura, Pressure dependence of magnetic states in Laves Phase RCo_2 (R = Dy, Ho, and Er) compounds probed by XMCD, *Journal of Physics: Conference Series* **190**, 012021 (2009).

[18] C. Giorgetti, S. Pizzini, E. Dartyge, A. Fontaine, F. Baudelet, C. Brouder, P. Bauer, G. Krill, S. Miraglia, D. Fruchart, and J. P. Kappler, Magnetic circular x-ray dichroism in Ce intermetallic compounds, *Physical Review B* **48**, 12732 (1993).

[19] A. Delobbe, A.-M. Dias, M. Finazzi, L. Stichauer, J.-P. Kappler, and G. Krill, X-ray magnetic circular dichroism study on $CeFe_2$, *Europhysics Letters* **43**, 320 (1998).

[20] J. Chaboy, M. A. Laguna-Marco, C. Piquer, H. Maruyama, and N. Kawamura, Relationship between XMCD and molecular field in rare-earth (R) transition-metal (T) intermetallic compounds, *Journal of Physics: Condensed Matter* **19**, 436225 (2007).

[21] T. Okane, Y. Takeda, H. Yamagami, A. Fujimori, Y. Matsumoto, N. Kimura, T. Komatsubara, and H. Aoki, Magnetic behavior near the boundary of 4f delocalization in ferromagnetic $CeRu_2Ge_2$ and paramagnetic $CeRu_2Si_2$ observed by Ce M_{4,5} XAS and XMCD, *Physical Review B* **86**, 125138 (2012).

[22] C. T. Chen, Y. U. Idzerda, H.-J. Lin, N. V. Smith, G. Meigs, E. Chaban, G. H. Ho, E. Pellegrin, and F. Sette, Experimental Confirmation of the X-Ray Magnetic Circular Dichroism Sum Rules for Iron and Cobalt, *Physical Review Letters* **75**, 152 (1995).

[23] B. T. Thole, G. Van Der Laan, J. C. Fuggle, G. A. Sawatzky, R. C. Karnatak, and J.-M. Esteva, 3d x-ray-absorption lines and the $3d^9$ 4f n^{+1} multiplets of the lanthanides, *Physical Review B* **32**, 5107 (1985).

[24] P. Carra, B. T. Thole, M. Altarelli, and X. Wang, X-ray circular dichroism and local magnetic fields, *Physical Review Letters* **70**, 694 (1993).

[25] R. Nakajima, J. Stöhr, and Y. U. Idzerda, Electron-yield saturation effects in L -edge x-ray magnetic circular dichroism spectra of Fe, Co, and Ni, *Physical Review B* **59**, 6421 (1999).

[26] J. P. Schillé, J. P. Kappler, P. Sainctavit, C. Cartier Dit Moulin, C. Brouder, and G. Krill, Experimental and calculated magnetic dichroism in the Ho 3d x-ray-absorption spectra of intermetallic $HoCo_2$, *Physical Review B* **48**, 9491 (1993).

[27] J. Stöhr and H. König, Determination of Spin- and Orbital-Moment Anisotropies in Transition Metals by Angle-Dependent X-Ray Magnetic Circular Dichroism, *Physical Review Letters* **75**, 3748 (1995).

[28] Y. Teramura, A. Tanaka, and T. Jo, Effect of Coulomb Interaction on the X-Ray Magnetic Circular Dichroism Spin Sum Rule in 3d Transition Elements, *Journal of the Physical Society of Japan* **65**, 1053 (1996).

[29] Y. Teramura, A. Tanaka, and T. Jo, Effect of Coulomb Interaction on the X-Ray Magnetic Circular Dichroism Spin Sum Rule in Rare Earths, *Journal of the Physical Society of Japan* **65**, 3056 (1996).

[30] T. Jo, The 3d–4f exchange interaction, X-ray second-order optical processes and the magnetic circular dichro-

ism (MCD) spin sum rule in rare earths, *Journal of Electron Spectroscopy and Related Phenomena* **86**, 73 (1997).

[31] V. G. Lunde, A. B. Møller, B. G. Eggert, A. M. Döring, J.-C. Grivel, R. Bjørk, F. Veillon, K. Skokov, O. Guttfleisch, A. O. Sjåstad, B. C. Hauback, and C. Frommen, Machine learning guided discovery and experimental validation of light rare earth Laves phases for magnetocaloric hydrogen liquefaction, *Acta Materialia* **297**, 121282 (2025).

[32] R. E. Dinnebier, A. Leineweber, and J. S. O. Evans, Rietveld refinement practical powder diffraction pattern analysis using topas, *Journal of Applied Crystallography* **52**, 1238 (2019).

[33] P. Ohresser, E. Otero, F. Choueikani, K. Chen, S. Stanescu, F. Deschamps, T. Moreno, F. Polack, B. Lagarde, J.-P. Daguerre, F. Marteau, F. Scheurer, L. Joly, J.-P. Kappler, B. Muller, O. Bunau, and P. Sainctavit, DEIMOS: A beamline dedicated to dichroism measurements in the 350–2500 eV energy range, *Review of Scientific Instruments* **85**, 013106 (2014).

[34] L. Joly, E. Otero, F. Choueikani, F. Marteau, L. Chappuis, and P. Ohresser, Fast continuous energy scan with dynamic coupling of the monochromator and undulator at the DEIMOS beamline, *Journal of Synchrotron Radiation* **21**, 502 (2014).

[35] G. Kresse and J. Furthmüller, Efficiency of *ab initio* total energy calculations for metals and semiconductors using a plane-wave basis set, *Computational Materials Science* **6**, 15 (1996).

[36] G. Kresse and J. Hafner, *Ab initio* molecular dynamics for liquid metals, *Physical Review B* **47**, 558 (1993), publisher: American Physical Society.

[37] G. Kresse and J. Furthmüller, Efficient iterative schemes for ab initio total-energy calculations using a plane-wave basis set, *Physical Review B* **54**, 11169 (1996), publisher: American Physical Society.

[38] D. Mejia-Rodriguez and S. B. Trickey, Deorbitalized meta-GGA exchange-correlation functionals in solids, *Physical Review B* **98**, 115161 (2018).

[39] H. J. Monkhorst and J. D. Pack, Special points for Brillouin-zone integrations, *Physical Review B* **13**, 5188 (1976), publisher: American Physical Society.

[40] M. Cococcioni and S. de Gironcoli, Linear response approach to the calculation of the effective interaction parameters in the LDA+U method, *Physical Review B* **71**, 035105 (2005), publisher: American Physical Society.

[41] M. W. Haverkort, G. Sangiovanni, P. Hansmann, A. Toschi, Y. Lu, and S. Macke, Bands, resonances, edge singularities and excitons in core level spectroscopy investigated within the dynamical mean-field theory, *Europhysics Letters* **108**, 57004 (2014), publisher: EDP Sciences, IOP Publishing and Società Italiana di Fisica.

[42] R. D. Cowan, Theoretical Calculation of Atomic Spectra Using Digital Computers*, *JOSA* **58**, 808 (1968).

[43] See Supplemental Material [url] for detailed methodology of multiplet theory simulations, Rietveld refinements of XRD data, additional XMCD and XAS spectra and hysteresis curves, and tabulated magnetic moments from sum rules and simulations.

[44] J. B. Goedkoop, B. T. Thole, G. Van Der Laan, G. A. Sawatzky, F. M. F. De Groot, and J. C. Fuggle, Calculations of magnetic x-ray dichroism in the 3d absorption spectra of rare-earth compounds, *Physical Review B* **37**, 2086 (1988).

[45] G. V. D. Laan, B. T. Thole, G. A. Sawatzky, J. C. Fuggle, and R. Karnatak, Identification of the relative population of spin-orbit split states in the ground state of a solid, *Journal of Physics C: Solid State Physics* **19**, 817 (1986).

[46] J. Farrell and W. E. Wallace, Magnetic Properties of Intermetallic Compounds between the Lanthanides and Nickel or Cobalt, *Inorganic Chemistry* **5**, 105 (1966).

[47] W. Wallace and K. Mader, Magnetic characteristics of $\text{Pr}_z \text{Y}_{1-z} \text{Ni}_2$ alloys and the nature of PrNi_2 at low temperatures, *Inorganic Chemistry* **7**, 1627 (1968).

[48] M. Ávila Gutiérrez, A. Moisset, A.-T. Ngo, S. Costanzo, G. Simon, P. Colombari, M. Petit, C. Petit, and I. Lisiecki, Influence of the nanocrystallinity on exchange bias in Co/CoO core/shell nanoparticles, *Colloids and Surfaces A: Physicochemical and Engineering Aspects* **676**, 132281 (2023).

[49] S. Blundell, *Magnetism in condensed matter*, Oxford master series in condensed matter physics (Oxford University Press, Oxford ; New York, 2001).

[50] A. Ermolenko, A. Korolev, E. Gerasimov, V. Gaviko, P. Terentev, and N. Mushnikov, Compositional genesis of ferromagnetism in alloys $\text{PrNi}_{2-x}\text{Co}_x$, *Journal of Magnetism and Magnetic Materials* **490**, 165489 (2019).

[51] Y. G. Xiao, Q. Huang, Z. W. Ouyang, F. W. Wang, J. W. Lynn, J. K. Liang, and G. H. Rao, Canted magnetic structure arising from rare-earth mixing in the Laves-phase compound $(\text{Nd}_{0.5}\text{Tb}_{0.5})\text{Co}_2$, *Physical Review B* **73**, 064413 (2006).

[52] B. K. Rai, A. D. Christianson, G. Sala, M. B. Stone, Y. Liu, and A. F. May, Magnetism of Nd_2O_3 single crystals near the Néel temperature, *Physical Review B* **102**, 054434 (2020).

[53] Y. Hinatsu and T. Fujino, Magnetic susceptibilities of $\text{UO}_2\text{-Pr}_2\text{O}_3$ solid solutions, *Journal of Solid State Chemistry* **74**, 163 (1988).

[54] W. Roth, The magnetic structure of Co_3O_4 , *Journal of Physics and Chemistry of Solids* **25**, 1 (1964).

[55] A. Mandziak, G. D. Soria, J. E. Prieto, P. Prieto, C. Granados-Miralles, A. Quesada, M. Foerster, L. Aballe, and J. de la Figuera, Tuning the Néel temperature in an antiferromagnet: the case of $\text{Ni}_x\text{Co}_{1-x}\text{O}$ microstructures, *Scientific Reports* **9**, 13584 (2019).

[56] C. Melcher, S. Friedrich, S. Cramer, M. Spurrier, P. Szupryczynski, and R. Nutt, Cerium oxidation state in LSO:Ce scintillators, *IEEE Transactions on Nuclear Science* **52**, 1809 (2005).

[57] H. B. Vasili, B. Casals, R. Cichelero, F. Macià, J. Geshev, P. Gargiani, M. Valvidares, J. Herrero-Martin, E. Pellegrin, J. Fontcuberta, and G. Herranz, Direct observation of multivalent states and $4f \rightarrow 3d$ charge transfer in Ce-doped yttrium iron garnet thin films, *Physical Review B* **96**, 014433 (2017).

[58] W. Liu, T. Gottschall, F. Scheibel, E. Bykov, N. Fortunato, A. Aubert, H. Zhang, K. Skokov, and O. Guttfleisch, Designing magnetocaloric materials for hydrogen liquefaction with light rare-earth Laves phases, *Journal of Physics: Energy* **5**, 034001 (2023).

[59] V. G. S. Lunde, Data for LIQUID-H (2025), dataVERSENO, doi: 10.18710/PT4R3F.

Supplemental material for "Electronic and magnetic properties of light rare-earth cubic Laves compounds derived from XMCD experiments"

Vilde G. S. Lunde,^{1,*} Benedicte S. Ofstad,¹ Øystein S. Fjellvåg,¹ Philippe Ohresser,² Anja O. Sjåstad,³ Bjørn C. Hauback,¹ and Christoph Frommen^{1,†}

¹*Department for Hydrogen Technology, Institute for Energy Technology, PO Box 40, NO-2027, Kjeller, Norway*

²*Synchrotron SOLEIL, L'Orme des Merisiers, 91190, Saint-Aubin, France*

³*Chemistry Department and Center for Material Science and Nanotechnology, University of Oslo, NO-0315, Norway*

(Dated: November 17, 2025)

This is the supplemental material. Section I provides a detailed description of the multiplet theory calculations performed, Section II contains refined XRD patterns with lattice constants in Section II, Section IV presents XAS and XMCD experimental and simulated spectra. Results from the sum rule calculations of XMCD data are in Section V.

I. MULTIPLET THEORY METHODOLOGY

QUANTY was used for full-multiplet calculations of the crystal electric field. Single-ion Hamiltonian, on-site Coulomb repulsion \mathcal{H}_U , in addition to the usual spin-orbit coupling \mathcal{H}_{SOC} , and a crystal electric field potential \mathcal{H}_{CEF} Hamiltonian:

$$\mathcal{H} = \mathcal{H}_U + \mathcal{H}_{SOC} + \mathcal{H}_{CEF}, \quad (A1)$$

$$= \mathcal{H}_U + \zeta \mathbf{L} \cdot \mathbf{S} + \sum_{l \in \{2,4,6\}} \sum_{m=-l}^l A_l^m C_l^m(\theta, \phi), \quad (A2)$$

with the coupling constant ζ of the orbital angular momentum \mathbf{L} , and spin angular momentum \mathbf{S} determined experimentally. \mathcal{H}_{CEF} is expanded over spherical harmonics $Y_l^m(\theta)$ with expansion coefficients A_l^m . We sum over the even orbital angular momentum quantum number l .

The crystal electric field was modeled assuming cubic point group symmetry, with the relevant expansion coefficients A_4^0 and A_6^0 treated as adjustable parameters for Nd and Pr as a cubic crystal field requires $A_4^{\pm 4} = \sqrt{\frac{5}{14}} A_4^0$ and $A_6^{\pm 4} = -\sqrt{\frac{7}{2}} A_6^0$. On the other hand, Ce has $J = 5/2$ and the expansion coefficients A_m^l can only act on a multiplet with m larger than $2J$. Thus, A_4^0 is the only free parameter for Ce. The correct crystal field parameters were identified by restricting the model to the XMCD spectra and the orbital moment, as determined by the orbital sum rules. As one or two parameters describe the crystal field, it is possible to find the global minimum. XAS and XMCD spectra were generated with a field of 5 T and a temperature of 4.2 K, as was done in the experiments.

* Contact author: vilde.lunde@ife.no

† Contact author: christoph.frommen@ife.no

II. X-RAY DIFFRACTION

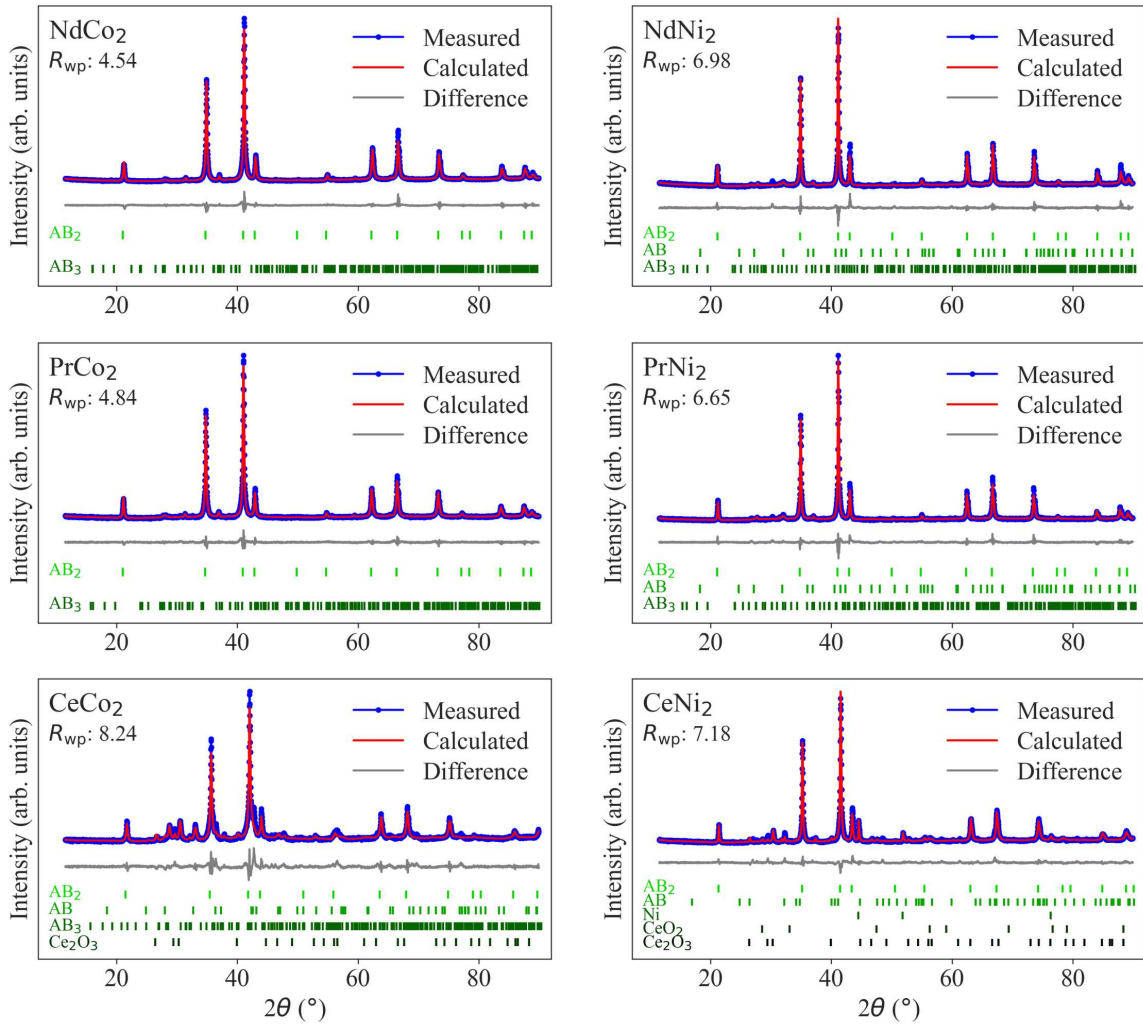


FIG. A1: Rietveld refinement of the XRD patterns of the reference samples, measured at room temperature, with a wavelength of 1.54060 Å. $K\beta$ was added due to imperfect $K\beta$ elimination by the detector.

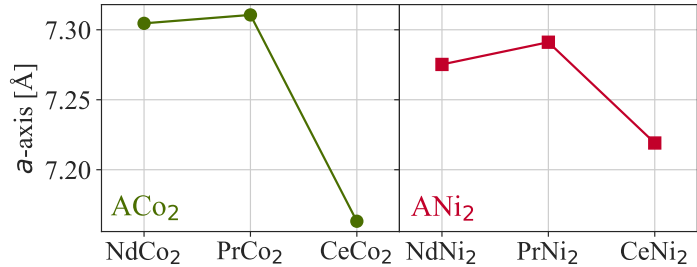


FIG. A2: Lattice constants for the AB_2 primary phase of the reference samples, based on Rietveld refinement of XRD-data, shown in Figure A1. Error bars are within the size of the markers.

III. DENSITY OF STATES

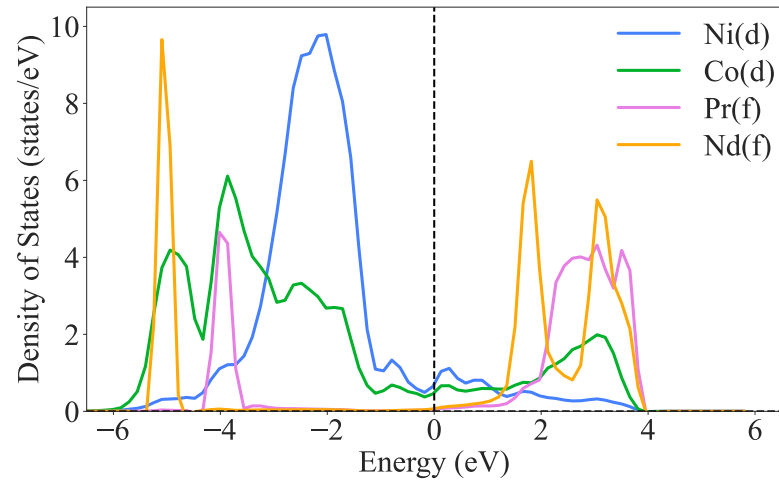


FIG. A3: Density of states for $\text{Nd}_{0.50}\text{Pr}_{0.50}\text{CoNi}$, generated using DFT. The Fermi energy is marked with a vertical dashed line.

IV. XAS AND XMCD SPECTRA

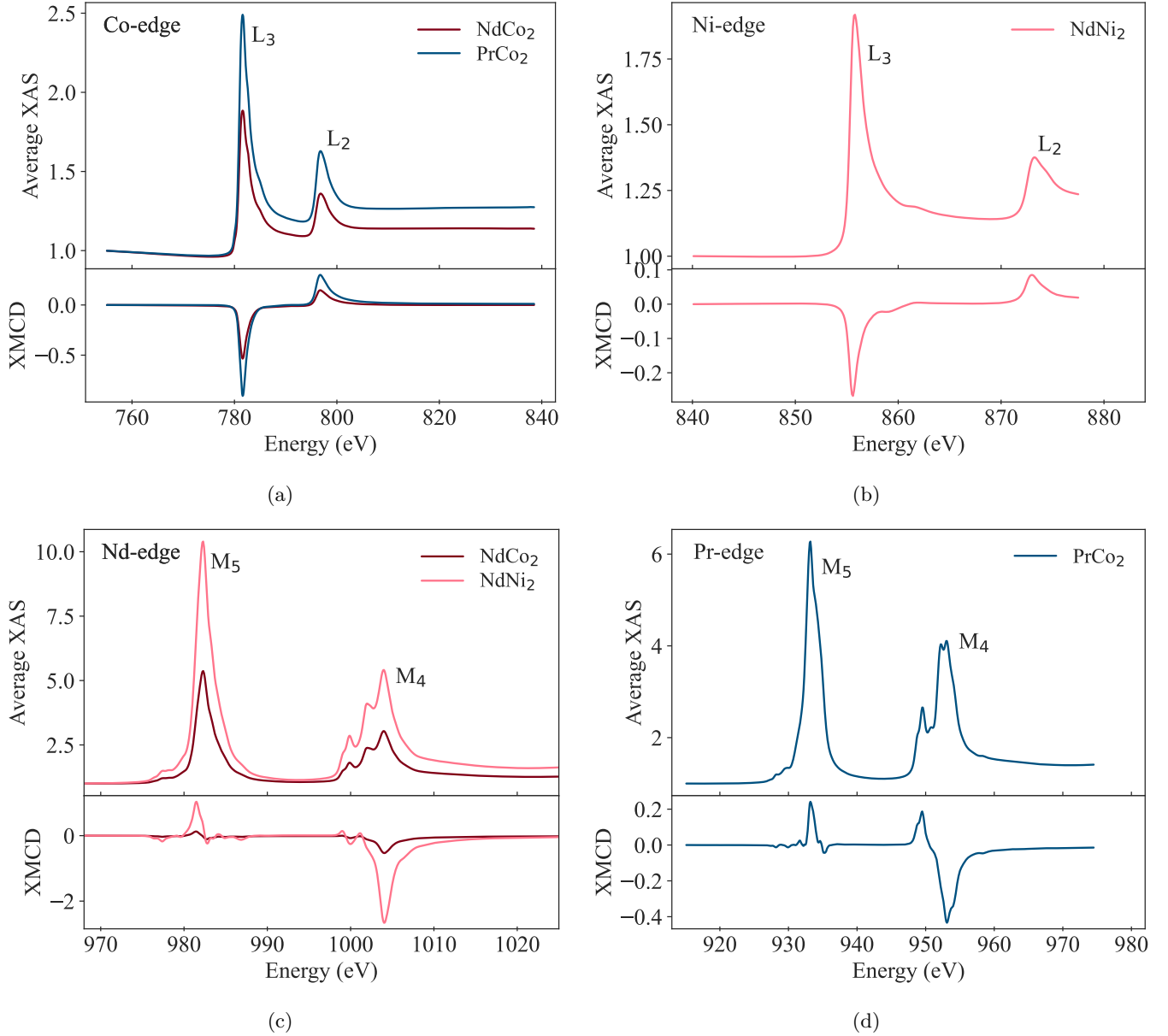


FIG. A4: XAS and XMCD for the binaries in a ferromagnetic state. Average XAS shows the average of the right and left polarized x-ray absorption, while XMCD shows the difference.

V. SUM RULES

TABLE A1: Orbital and spin magnetic moments at 4.2 K and 5 T calculated using the magneto-optical sum rules. n_h was calculated using DFT. Values for binaries in a ferromagnetic state are included. Values calculated using the spin sum rule for the rare earth elements are written in cursive to underline their invalidity.

Composition	Atom	n_h	μ_L (μ_B /atom)	μ_S (μ_B /atom)	μ_{tot} (μ_B /atom)	μ_L/μ_S
NdCo ₂	Co	1.56	0.23	1.05	1.28	0.22
PrCo ₂	Co	1.56	0.10	1.22	1.32	0.08
NdCoNi	Co	1.56	0.15	1.18	1.32	0.12
Nd _{0.75} Pr _{0.25} CoNi	Co	1.56	0.07	1.11	1.18	0.06
Nd _{0.50} Pr _{0.50} CoNi	Co	1.56	0.09	1.32	1.41	0.07
Nd _{0.25} Pr _{0.75} CoNi	Co	1.56	0.12	1.17	1.29	0.10
PrCoNi	Co	1.56	0.14	1.28	1.42	0.11
Ce _{0.25} Pr _{0.75} CoNi	Co	1.56	0.16	1.13	1.29	0.14
NdNi ₂	Ni	1.07	0.07	0.34	0.41	0.20
NdCoNi	Ni	1.07	0.06	0.54	0.60	0.11
PrCoNi	Ni	1.07	0.05	0.56	0.61	0.09
NdCo ₂	Nd	11.00	1.28	1.58*	-0.30*	0.81*
NdNi ₂	Nd	11.00	1.94	3.24*	-1.31*	0.60*
NdCoNi	Nd	11.00	1.69	2.80*	-1.11*	0.60*
Nd _{0.75} Pr _{0.25} CoNi	Nd	11.00	1.46	3.01*	-1.55*	0.49*
Nd _{0.50} Pr _{0.50} CoNi	Nd	11.00	1.68	3.27*	-1.59*	0.51*
Nd _{0.25} Pr _{0.75} CoNi	Nd	11.00	1.19	2.95*	-1.75*	0.41*
PrCo ₂	Pr	12.00	0.25	0.72*	-0.47*	0.35*
Nd _{0.75} Pr _{0.25} CoNi	Pr	12.00	0.31	1.32*	-1.00*	0.24*
Nd _{0.50} Pr _{0.50} CoNi	Pr	12.00	0.54	1.35*	-0.81*	0.40*
Nd _{0.25} Pr _{0.75} CoNi	Pr	12.00	0.55	1.25*	-0.70*	0.44*
PrCoNi	Pr	12.00	0.49	1.32*	-0.83*	0.37*
Ce _{0.25} Pr _{0.75} CoNi	Pr	12.00	0.55	1.25*	-0.70*	0.44*
Ce _{0.25} Pr _{0.75} CoNi	Ce	13.00	0.53	0.68*	-0.15*	0.77*

*Calculated using the invalid spin sum rule for 4f elements.

TABLE A2: Orbital and spin magnetic moments at 4.2 K and 5 T calculated using multiplet theory. Parameters were chosen so that μ_L was the same as the experimental, and these parameters were used to calculate μ_S .

Composition	Atom	n_h	μ_L (μ_B /atom)	μ_S (μ_B /atom)	μ_{tot} (μ_B /atom)	μ_L/μ_S
NdCo ₂	Nd	11.00	1.28	0.32	0.96	4
NdNi ₂	Nd	11.00	1.94	0.48	1.45	4
NdCoNi	Nd	11.00	1.69	0.42	1.26	4
Nd _{0.75} Pr _{0.25} CoNi	Nd	11.00	1.46	0.36	1.09	4
Nd _{0.50} Pr _{0.50} CoNi	Nd	11.00	1.68	0.42	1.26	4
Nd _{0.25} Pr _{0.75} CoNi	Nd	11.00	1.19	0.30	0.89	4
PrCo ₂	Pr	12.00	0.25	0.06	0.19	4
Nd _{0.75} Pr _{0.25} CoNi	Pr	12.00	0.31	0.08	0.24	4
Nd _{0.50} Pr _{0.50} CoNi	Pr	12.00	0.54	0.13	0.40	4
Nd _{0.25} Pr _{0.75} CoNi	Pr	12.00	0.55	0.14	0.41	4
PrCoNi	Pr	12.00	0.49	0.12	0.37	4
Ce _{0.25} Pr _{0.75} CoNi	Pr	12.00	0.55	0.14	0.41	4
Ce _{0.25} Pr _{0.75} CoNi	Ce	13.00	0.53	0.13	0.40	4